

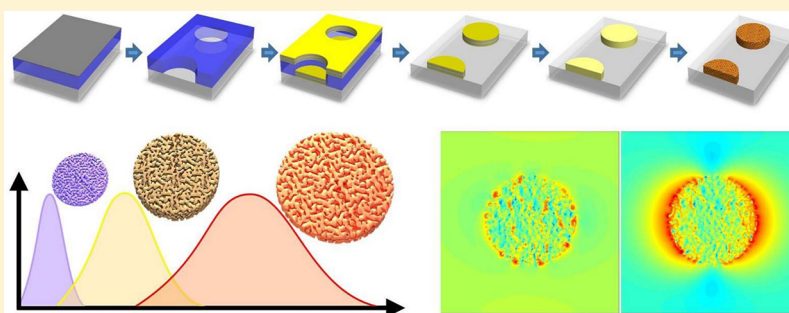
EBL-Based Fabrication and Different Modeling Approaches for Nanoporous Gold Nanodisks

Md Masud Parvez Arnob,^{†,‡} Fusheng Zhao,^{†,‡} Jingting Li,[†] and Wei-Chuan Shih^{*,†,‡,§,||,#}

[†]Department of Electrical and Computer Engineering, [‡]Department of Biomedical Engineering, [§]Program of Materials Science and Engineering, and ^{||}Department of Chemistry, University of Houston, Houston, Texas 77204, United States

[#]Biomedical Institute for Global Health Research and Technology (BIGHEART), National University of Singapore, 14 Medical Drive, Singapore 117599

Supporting Information



ABSTRACT: We report electron beam lithography (EBL) based fabrication and different modeling techniques for disk-shaped nanoporous gold nanoparticles (NPG disk). The EBL technique can provide large area 2D patterns of regularly or randomly distributed nanodisks with narrow size distribution and flexible interdisk (center to center) distance. Such flexibility is essential to obtain quasi-single NPG disk response, which typically peaks in the near-infrared (NIR) spectrum beyond 1 μm , from ensemble measurements by common UV/vis/NIR spectrometers instead of a specialized NIR spectroscopic microscope. NPG disks of 200 to 500 nm diameter and 50 nm thickness have been fabricated and characterized. To model the NPG disk and calculate its plasmonic properties, two different modeling approaches have been developed. A model based on the Bruggeman effective medium theory (B-EMT model) requires little information about the nanoporous structure. In contrast, the nanoporous model (NP model) retains the essential nanoporous structural features of NPG disk. To evaluate the performance of these models, simulated extinction spectra have been compared to the experimental data. Both the B-EMT and NP models perform well to estimate the far-field plasmon resonance peak position. However, to obtain the accurate information about the plasmon peak width/plasmon lifetime and near-field plasmonic hot-spots formation within the nanopores, the NP model is essential since the B-EMT model lacks the nanoporous network.

KEYWORDS: plasmonic nanoparticles, nanoporous gold nanoparticles, numerical modeling, effective medium approximation

Light excited nonpropagating resonant oscillation of conduction band electrons, known as localized surface plasmon resonance (LSPR), has made metallic nanoparticles a recent research focus. Through advances in fabrication, surface functionalization, and assembly, plasmonic properties of metallic nanoparticles have impacted fields such as imaging labels, catalysis, biochemical sensors, and surface-enhanced spectroscopies.^{1,2} While LSPR can be found in most metallic nanoparticles, silver and gold are the commonly used materials, as their plasmon resonances are within the visible range. Gold nanoparticles, in particular, offer several advantages such as biocompatibility, chemical inertness, and convenience of surface functionalization over other metals.¹ Among various gold nanoparticles, disk-shaped nanoporous gold (NPG) nanoparticles, also known as NPG disks, are a novel class of plasmonic nanoparticles featuring many interesting properties.^{3,4} For example, it provides significant local field enhance-

ment by 3-dimensionally distributed, high-density “hot-spots”. Furthermore, the porous network provides larger specific surface area compared to other bulk nanoparticles with similar dimensions. These superior properties have made NPG disk a promising material for sensing, imaging, and photothermal applications.^{5–9}

The effectiveness of NPG disks in different applications depends on their plasmonic properties, which are controlled by the physical dimensions and local dielectric environment.^{10,11} Thus, having a comprehensive understanding of the NPG disk plasmonics is of paramount importance for optimization of specific applications. The complete understanding of NPG disk plasmonics methodically requires the experimental and theoretically calculated (that requires the particle modeling

Received: March 10, 2017

Published: June 12, 2017

beforehand) data for single NPG disk, which are the primary focuses of this study.

Conventionally, dark-field scattering microscopy can be used to obtain single NPG disk response. For example, Vidal et al. acquired the single spheroidal NPG nanoparticle (made by dewetting/dealloying process) response via dark field scattering measurement.¹² The fabricated nanoparticles were irregular in shape, but of similar diameter (~ 205 nm), and the scattering maxima varied between 790 to 905 nm depending on the specific 3D pore-ligament network. However, for the NPG disk, the LSPR peak typically locates beyond $1 \mu\text{m}$ wavelength, and hence, a specialized near-infrared (NIR) dark-field microscope is required. Besides the dark-field scattering technique, spatial modulation spectroscopy, and photothermal imaging technique can be employed to obtain single nanoparticle response.¹³ However, these techniques are complicated in nature, and the latter is very inefficient for materials with dominant radiative plasmon decay channels. Simple ensemble measurements from the common UV/vis/NIR spectrometer can also be used to obtain quasi-single nanoparticle response if the nanoparticles are randomly distributed with large center to center (~ 6 particle diameter) distance and have very narrow size distribution.¹⁴ The random arrangement, together with the large interparticle distance, nullifies the particle–particle coupling effects. In the past, nanosphere lithography has been employed by our group to fabricate random NPG disk arrays.^{3,15} However, the as-fabricated disk arrays exhibit interparticle distance much less than 6, thereby preventing single disk response. In addition, NSL is known to produce less monodisperse particles compared to electron beam lithography (EBL). It is our aim to develop EBL compatible technique to pattern randomly distributed sparse (large interparticle distance) arrays with narrow size distribution to obtain quasi-single nanoparticle response using the common UV/vis/NIR spectrometer.

Several methods have been reported in the literature for NPG nanoparticle fabrication. Wang et al. reported a thermal dewetting process,¹⁶ however, the fabricated nanoparticles are highly irregular in shape and size with ~ 100 nm standard deviation in the particle diameter. Zhao et al. fabricated semirandomly distributed NPG disk arrays using nanosphere lithography to pattern Au–Ag alloy disks followed by dealloying.⁵ This method provides limited control over the interparticle (center to center) distance which typically is too small to avoid far-field coupling. Wi et al. reported the fabrication of periodic porous gold nanodisks by dealloying EBL made Au–Cu alloy disks.¹⁷ The fabricated porous disks were irregular in shape and lacked the three-dimensional (3D) bicontinuous porous network. Besides, the periodic disk array provided a grating effect in the particle response. Liu et al. reported a colloidal synthesis technique of making porous Au–Ag nanospheres that produced broad particle size distribution.¹⁰ Hence, a method is required to fabricate NPG disks with well-controlled size, shape, and locations.

In the literature, there have been several efforts to model NPG nanostructure. Sardana et al. used the Bruggeman effective medium theory (B-EMT) to model 50 nm thick NPG film with pore size ranging from 12 to 30 nm to calculate the dispersion relation of propagating surface plasmon.¹⁸ Similarly, Dixon et al. employed the B-EMT model for ~ 40 to 1600 nm thick NPG film to calculate the real and imaginary refractive indices.¹⁹ Results from these studies were in good agreement with experimental data. However, the B-EMT model

does not consider the nanoporous architecture, which contains the significant near-field information. Ngo et al. used molecular dynamics simulation to model the porous network of the NPG film with ligament size of ~ 3.15 nm.²⁰ Erlebacher et al. also modeled the NPG nanostructure (~ 2 to 5 nm ligament width) by employing the kinetic Monte Carlo simulation.²¹ Both of these models provided key understanding of the physical and mechanical properties of the porous film. Yet, there has been no effort to calculate the plasmonic properties using these techniques. Besides, both approaches require highly specialized computational skills and significant amount of time to generate the model.²² Lang et al. used a simplified porous model for NPG film to calculate the extinction spectrum and electric field (e-field) enhancement.²³ The model consists of a 2D periodic hexagonal array of nanoholes with edge to edge distance corresponding to the ligament width. The periodicity of the array and the through-all nanohole significantly deviate from the actual NPG bicontinuous structure. Besides NPG films, NPG nanoparticles have also been modeled in several previous studies. Arnob et al. employed the Maxwell-Garnett effective medium theory to model the NPG disk and calculate its extinction properties.²⁴ However, due to the absence of the 3D porous network, this model is not suitable for near-field investigations. Wi et al. used scanning electron microscope (SEM) images to model porous gold nanodisk to calculate the e-field distribution.¹⁷ Zhang et al. modeled the quasi-spherical porous Au nanoparticle using a Au sphere with a varying number of pores randomly generated at the particle surface.²⁵ Both of these models are 2D in nature and do not contain the essential 3D bicontinuous pore-ligament network of NPG. Liu et al. reported a 3D model of porous Au–Ag nanosphere to calculate the extinction spectra and e-field distribution.¹⁰ However, this model is not described in detail, and to authors' inference, it has a periodic pore-ligament network that deviates from the random nature of NPG architecture. Besides, all the models were developed to obtain a qualitative understanding of the plasmonic properties. There has been no quantitative performance evaluation for the proposed models.

In this paper, we present new fabrication and modeling techniques for NPG disks adhering to the lay out as follows: An EBL-based fabrication technique will first be presented for NPG structures of arbitrary shapes and patterns. This technique will be applied to fabricate randomly distributed NPG disk arrays with large interdisk distance to minimize the coupling effects, thereby making it possible to obtain quasi-single disk response using a UV/vis/NIR spectrometer.¹⁴ Two different modeling approaches (B-EMT and NP) will then be presented. Finite difference time domain (FDTD) method and analytical oblate spheroid theory (OST) will be employed in calculations. To evaluate the performance of these models, simulated extinction spectra will be compared to experimentally measured data for 200 to 500 nm diameter and 50 nm thick NPG disks.

RESULTS AND DISCUSSION

EBL-Fabricated NPG Disks. Figure 1a shows the SEM image of periodic NPG disk arrays (300 nm diameter and 80 nm thickness) with two different pitches (0.8 and 1.3 μm). Figure 1b presents the periodic NPG disk arrays of different diameter (200, 300, 400, and 500 nm). The EBL method is versatile and capable of fabricating NPG structure of any arbitrary shapes and patterns. Figure 1c–f shows the NPG structures of “square”, “hollow-square”, and “triangular” shapes and “UH” patterns, respectively.

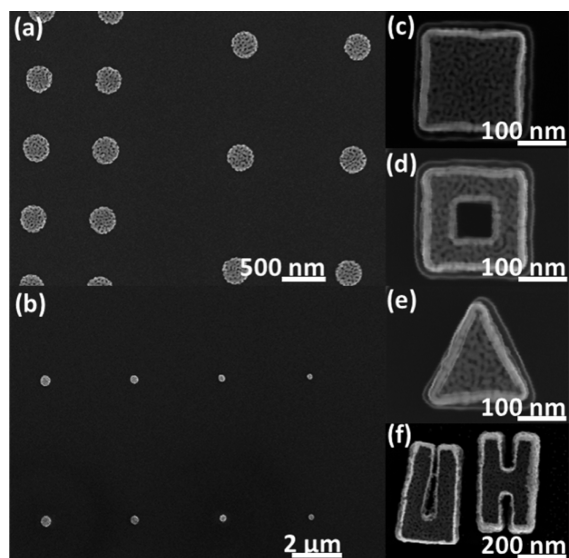


Figure 1. (a) Periodic arrays of 300 nm diameter NPG disks with two different interdisk distances (0.8 and 1.3 μm). (b) Periodic array of NPG disks of different diameter (200–500 nm). NPG structure of (c) “square”, (d) “hollow-square”, (e) “triangular” shapes, and (f) “UH” pattern.

Although the EBL method is traditionally used to fabricate periodic arrays, in this study we utilize this method to fabricate randomly distributed NPG disks to obtain coupling-free quasi-single particle response using the common UV/vis/NIR

spectrometer. Figure 2a–d shows the SEM images of 200, 300, 400, and 500 nm diameter (average) NPG disks, respectively. The corresponding random disk arrays are shown in Figure 2e–h. Figure 2i–l presents the corresponding Fourier transform (FT) images. The absence of discrete spots and the appearance of more salient ring-shaped patterns justify the randomness of the fabricated disk array. The small variation in nanodisk diameter is supported by the corresponding size distribution histograms in Figure 2m–p. The size distribution histograms were obtained by analyzing several SEM images (ImageJ), summing up to about 70 analyzed disks for each size. In general, the distribution has a relative standard deviation (RSD) of $\sim 7\%$.

Plasmonic Extinction Spectra. Figure 3 presents the dielectric permittivities of bulk gold and NPG structure. The

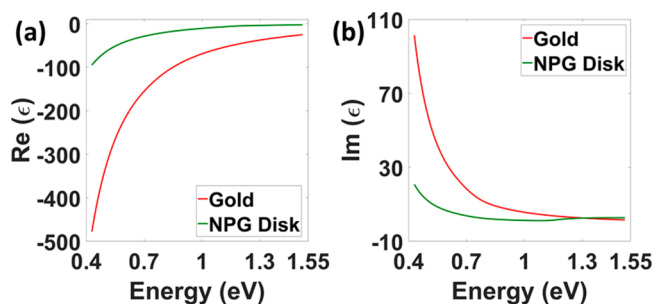


Figure 3. (a) Real and (b) imaginary part of dielectric permittivity of bulk gold and NPG structure.

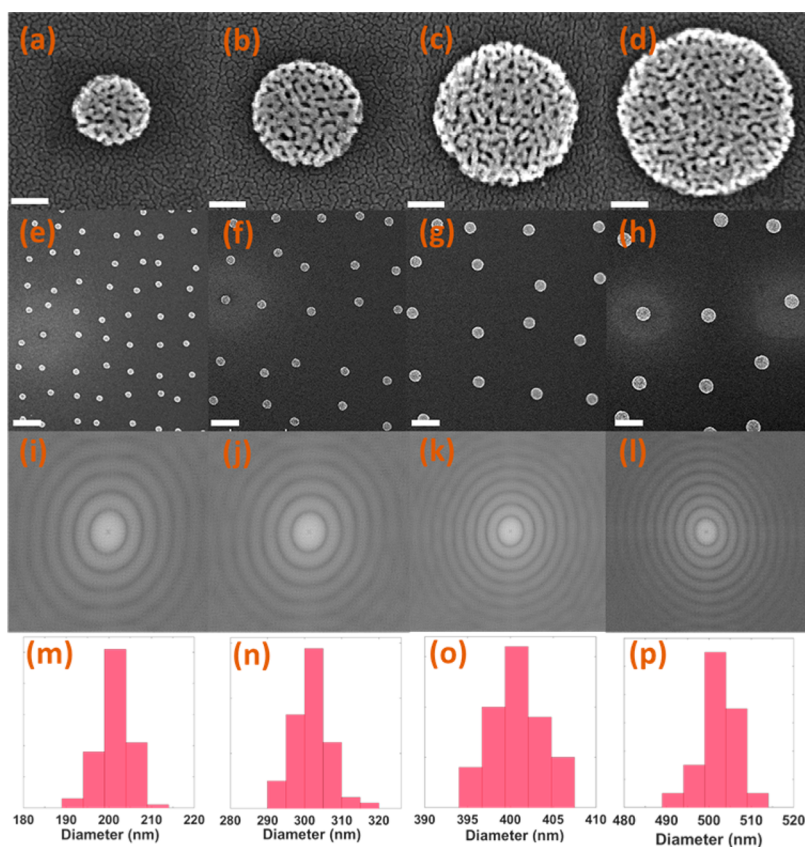


Figure 2. (a–d) SEM images of 200, 300, 400, and 500 nm diameter (average) NPG disks, respectively. The scale bar is 100 nm. (e–h) SEM images of the corresponding NPG disk arrays (randomly distributed). The scale bar is 1 μm . (i–l) Corresponding FT images showing the ring-shaped patterns. (m–p) Corresponding size distribution histograms.

gold permittivity is obtained from the experimental measurement by Johnson and Christy,²⁶ while the permittivity of the NPG structure is calculated by the B-EMT model. As shown in Figure 3a,b, both the real and imaginary parts are different for the bulk gold and NPG structure, thereby highlighting their optical difference and validating the B-EMT modeling as well.

Figure 4a shows the experimental extinction spectra of 200, 300, 400, and 500 nm diameter NPG disks of 50 nm thickness.

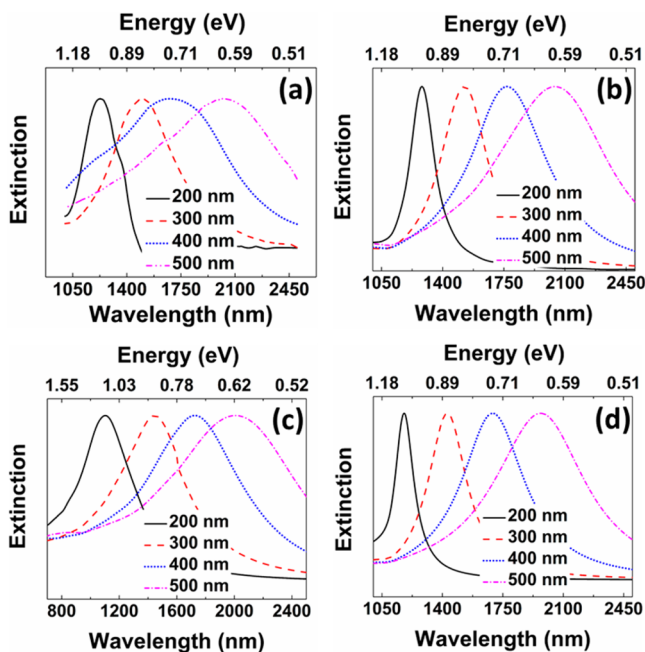


Figure 4. Extinction spectra of 200, 300, 400, and 500 nm diameter NPG disks: (a) Experiment, (b) B-EMT model/FDTD calculation, (c) NP model/FDTD calculation, and (d) B-EMT model/OST calculation.

Figure 4b and c display the FDTD calculated extinction spectra for the corresponding B-EMT and NP models of NPG disks, respectively. Figure 4d presents the OST calculated extinction spectra for the B-EMT model. The B-EMT model is very simple and the analytical OST can be employed to calculate the plasmonic properties, which is not possible for the NP model. The extinction spectra of NPG disks feature an in-plane dipolar LSPR peak (λ_{LSPR} (nm)/ E_{LSPR} (eV) and the full width at half-maximum (fwhm). Figure 5a depicts the variations of E_{LSPR} with respect to different disk diameter as calculated and experimentally observed. The numeric LSPR peak values are listed in Table 1. We find an excellent agreement between the experimental data and the calculations. This observation

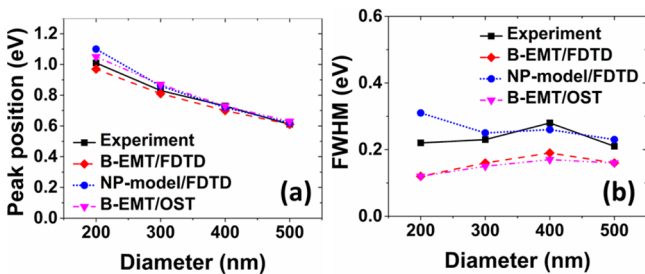


Figure 5. Diameter dependent variations of (a) LSPR peak position and (b) fwhm.

confirms the anticipated possibility to experimentally obtain ensemble-single particle response by extinction on EBL fabricated random arrangements of sparse nanodisks. The trend of an increasing difference between the model and experiments, for decreasing disk size, is a consequence of increasing relative polydispersity for smaller disks. Size-dependent LSPR tuning has also been reported for other porous nanoparticles. Zhang et al. varied the mean diameter of colloidal porous Au nanoparticles and obtained the LSPR peak shift.²⁵ Similarly, Rao et al. tuned the LSPR peak for spheroidal NPG nanoparticles by changing its average diameter.¹¹ In both cases, alike NPG disk, the LSPR peak red-shifted with increasing particle size due to the retardation effect.

Figure 5b presents the experimentally observed and calculated diameter dependence of the fwhm for NPG disks of different diameter. The numeric fwhm values are enlisted in Table 1. The fwhm is related to the plasmon lifetime, T by $T = \hbar/\text{fwhm}$, where \hbar is the normalized Planck's constant.^{27,28} Table 1 lists the calculated plasmon lifetime for the corresponding fwhm values. Quantitatively, plasmon lifetime calculated from the NP model agrees much better with the experimental data. In contrast, the lifetime obtained from the B-EMT model are significantly longer. A plausible explanation is that the porous network increases the probability of electron collisions, causing enhanced plasmon damping and the shortened lifetime.²⁵ The small quantitative difference between the models and experiments can be attributed to porosity (δ_{air}) mismatch, inaccurate substrate effect modeling, and the heterogeneous particle dimensions.¹¹

The effect of δ_{air} on the LSPR peak position is depicted in Figure 6. Figure 6a, b, and c present the variations of E_{LSPR} (eV) with respect to different δ_{air} values for B-EMT model/FDTD calculation, NP model/FDTD calculation, and B-EMT model/OST calculation, respectively. With increasing δ_{air} values, the LSPR peak positions are red-shifted toward the experimental observations. This suggests that a better peak position match can be obtained by slightly tuning the δ_{air} for each disk dimension. Upon comparison with the experimental data, the calculated δ_{air} (0.54) appears to be more accurate for the larger disk diameters. Figure 6 also hints the applicability of δ_{air} as an additional tuning factor for E_{LSPR} in addition to the particle dimension and surrounding environment. Zhang et al. reported the variation in LSPR peak position with respect to different porosity values for colloidal Au nanoparticle.²⁵ Rao et al. also presented the LSPR peak tuning by varying the porosity level in spheroidal NPG nanoparticles.¹¹ In both cases, the LSPR peak became red-shifted with increasing porosity, which is in consistent with that for the NPG disk.

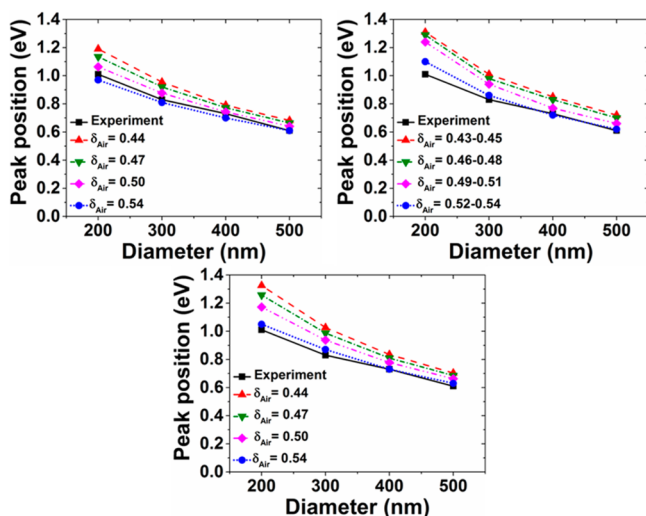
As depicted in Figures 5a and 6, if the diameter increases, the LSPR energy shifts into the red. The diameter dependent LSPR shift can be understood mathematically by the polarizability equation for NPG disk. According to the modified long wavelength approximation (MLWA),¹⁴ the polarizability for NPG disk can be expressed as

$$\alpha'(\omega) = \frac{\pi D^2 T}{6} \times \frac{\delta_{\text{air}} \omega_p^2}{\left[L \delta_{\text{air}} \omega_p^2 - \omega^2 \left(1 + \frac{\delta_{\text{air}} \omega_p^2}{12c^2} DT \right) \right] - i\omega \left(\gamma + \frac{\delta_{\text{air}} \omega_p^2}{36c^3} D^2 T \right)} \quad (1)$$

In this expression, D and T are the disk diameter and thickness, respectively, ω_p is the bulk plasmon frequency, γ is

Table 1. Experimentally Observed and Calculated Diameter (D) Dependent λ_{LSPR} (nm)/ E_{LSPR} (eV) and fwhm (eV)/ T (fs) Values

D (nm)	λ_{LSPR} (nm)/ E_{LSPR} (eV)				fwhm (eV)/ T (fs)			
	expt	B-EMT (FDTD)	B-EMT (OST)	NP model (FDTD)	expt	B-EMT (FDTD)	B-EMT (OST)	NP model (FDTD)
200	1228/1.01	1278/0.97	1181/1.05	1127/1.10	0.22/2.99	0.12/5.49	0.12/5.49	0.31/2.13
300	1500/0.83	1525/0.81	1429/0.87	1447/0.86	0.23/2.86	0.16/4.12	0.15/4.39	0.25/2.64
400	1698/0.73	1770/0.70	1698/0.73	1723/0.72	0.28/2.35	0.19/3.47	0.17/3.87	0.26/2.53
500	2032/0.61	2035/0.61	1971/0.63	2004/0.62	0.21/3.14	0.16/4.12	0.16/4.12	0.23/2.86

**Figure 6.** Variations of E_{LSPR} for different δ_{air} values for (a) B-EMT model/FDTD calculation, (b) NP model/FDTD calculation, and (c) B-EMT model/OST calculation. Four different δ_{air} values are used. For the B-EMT model, $\delta_{\text{air}} = 0.44, 0.47, 0.5, \text{ and } 0.54$. For the NP model, $\delta_{\text{air}} = 0.43\text{--}0.45, 0.46\text{--}0.48, 0.49\text{--}0.51, \text{ and } 0.52\text{--}0.54$.

the interband damping, and L ($\sim \pi T/4D$) is the depolarization factor. The real part of the pole of eq 1 defines the localized surface plasmon frequency ω_{LSPR} as

$$\omega_{\text{LSPR}}^2 = \frac{\pi \delta_{\text{Au}} \omega_{\text{p}}^2}{\frac{4D}{h} + \frac{\delta_{\text{Au}} \omega_{\text{p}}^2}{12c^2} D^2} \quad (2)$$

Since $E_{\text{LSPR}} = \hbar \omega_{\text{LSPR}}$, eq 2 explains the $1/D$ dependence of E_{LSPR} . Equation 2 also explains the δ_{air} dependent LSPR peak shift. With increasing δ_{air} values, δ_{Au} decreases, and thus LSPR peak is red-shifted. As shown in Figure 5b, for 200–400 nm diameter NPG disks, the fwhm increases with increasing disk diameter. However, for 500 nm diameter disk, the fwhm is smaller than that for 400 nm diameter. To understand these increase and decrease phenomena, we need to consider the origin of fwhm. The fwhm can be assumed as the sum of three separate contributions, intraband damping, interband damping, and radiation damping.²⁷ Since the LSPR energies for NPG disks are far below the interband threshold (2.3 eV for Au), the interband damping contribution is negligible.¹⁴ Further, the intraband damping has a very weak diameter dependence at constant temperature. Thus, the fwhm for NPG disks is dominated by the radiation damping, which depends on the disk volume. As the diameter increases, the disk volume and the size of the induced dipole increase, thereby enhancing radiation damping and hence the fwhm increases. This is the super radiant regime. However, when the size of the nanodisk becomes comparable to the excitation wavelength, it enters into the subradiant/quenched radiation regime, where the electrons

begin to oscillate out of phase, thereby diminishing the dipole radiation strength.²⁹ In this regime the fwhm decreases with increasing disk diameter. NPG disk enters into the subradiant regime for a diameter larger than 400 nm, and hence, the fwhm decreases with further diameter increase. The diameter dependent fwhm variations can also be understood by the polarizability equation (eq 1), which can be rewritten as

$$\alpha'(\omega) = \frac{\pi D^2 T}{6} \times \frac{\frac{\delta_{\text{Au}} \omega_{\text{p}}^2}{1 + \frac{\delta_{\text{Au}} \omega_{\text{p}}^2}{12c^2} DT}}{\frac{L \delta_{\text{Au}} \omega_{\text{p}}^2}{1 + \frac{\delta_{\text{Au}} \omega_{\text{p}}^2}{12c^2} DT} - \omega^2 - i\omega \frac{\left(\gamma + \frac{\delta_{\text{Au}} \omega_{\text{p}}^2 \omega^2}{36c^3} - D^2 T\right)}{\frac{L \delta_{\text{Au}} \omega_{\text{p}}^2}{1 + \frac{\delta_{\text{Au}} \omega_{\text{p}}^2}{12c^2} DT} - \omega^2}} \quad (3)$$

The fwhm can be written as (neglecting γ)

$$\text{fwhm} = \frac{\delta_{\text{Au}} \omega_{\text{p}}^2 \omega_{\text{LSPR}}^2 D^2 T}{36c^3} \frac{1}{1 + \frac{\delta_{\text{Au}} \omega_{\text{p}}^2}{12c^2} DT} \quad (4)$$

For the small particle limit, $\delta_{\text{Au}} \omega_{\text{p}}^2 DT/12c^2 \ll 1$, and ω_{LSPR}^2 is equal to $L \delta_{\text{Au}} \omega_{\text{p}}^2$ (eq 3). Thus, since $L \propto 1/D$, $\text{fwhm} \propto \delta_{\text{Au}}^2 \omega_{\text{p}}^2 D$, that is, as the disk diameter increases, fwhm increases. For the large particle limit, $\delta_{\text{Au}} \omega_{\text{p}}^2 DT/12c^2 \gg 1$ and $\text{fwhm} \propto \omega_{\text{LSPR}}^2 D$. Furthermore, since, in this limit, $\omega_{\text{LSPR}}^2 \propto 1/D^2$, $\text{fwhm} \propto 1/D$, that is, fwhm decreases with increasing disk diameter.

Plasmonic Hot-Spots. Figure 7a,b shows the calculated e-field distributions at λ_{LSPR} for the B-EMT and NP models of 300 nm diameter and 50 nm thick NPG disk, respectively. The field distributions are recorded on the top surface where incident light impinges. For the NP model, hot-spot distribution appears to be concentrated near the pores around edges, denoting the coupling between the in-plane resonance and the pores around edges. However, although the B-EMT model can predict the in-plane field distribution around the edges, the coupling feature is missing. Figure 7c,d depicts the field distributions at 785 nm wavelength for the B-EMT and NP model, respectively. For the NP model, densely distributed plasmonic hot-spots appear in the porous network. The B-EMT model does not account for the internal hot-spots due to the lack of porous architecture in the model. Since NPG disk contains the 3D bicontinuous pore-ligament network, obtaining e-field distributions along different cross sections facilitates the understanding of hot-spots formation. Figure 8a–c shows the e-field distributions across the disk diameter (x – y cross-section) at three different z positions (height). All the calculations are for 300 nm diameter and 50 nm thick NPG disk NP model at 785 nm excitation wavelength. Details of the varying e-field distributions along the z dimension (at 1 nm step size) is provided in visualization 3 (Supporting

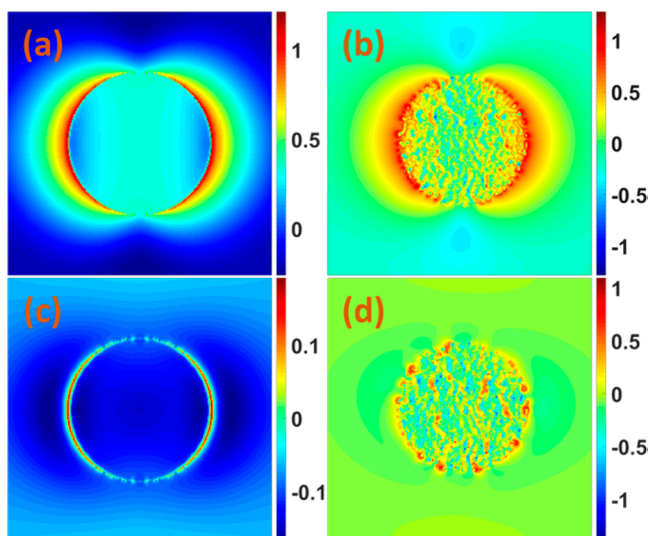


Figure 7. Calculated e-field distributions on the top surface of 300 nm diameter and 50 nm thick NPG disk models: (a) B-EMT model ($\lambda_{\text{LSPR}} = 1225$ nm), (b) NP model ($\lambda_{\text{LSPR}} = 1447$ nm), (c) B-EMT model ($\lambda = 785$ nm), and (d) NP model ($\lambda = 785$ nm). The color bar represents the \log_{10} values.

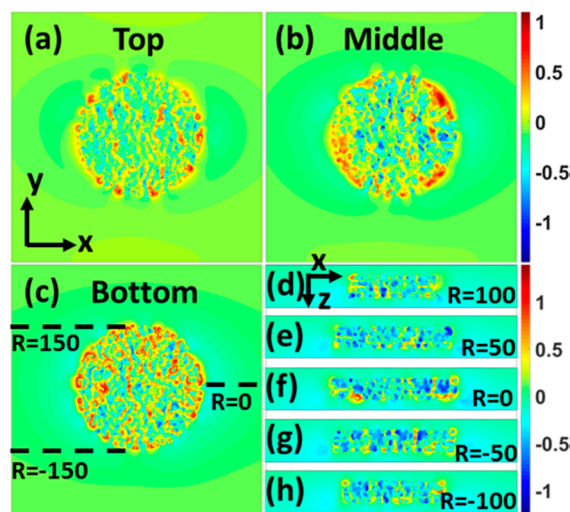


Figure 8. (a–c) Calculated e-field distributions for 300 nm diameter and 50 nm thick NPG disk NP model at top, middle, and bottom x – y cross sections. (d–h) Calculated e-field distributions at the x – z cross sections for $R = 100, 50, 0, -50,$ and -100 . The excitation wavelength is $\lambda = 785$ nm. The color bar represents the \log_{10} values.

Information). Figure 8d–h shows the e-field distributions at the x – z cross-section at six different radial positions. More detailed representations (e-field distribution at 5 nm step size) are provided in a movie in visualization 4 (Supporting Information). Plasmonic hot-spots are distributed three dimensionally inside the NPG disk. The field enhancement is larger at the particle–substrate interface. Similar behavior was observed by Hagglund et al. for Au nanodisks, who attributed the behavior to two asymmetric dipoles, localized at the air and substrate side of the particle, dominated by the substrate dipole.³⁰ The e-field distribution and enhancement is random in nature due to the random pore–ligament structure.

Calculation Time and Memory. The B-EMT model is symmetric in both x and y directions. Hence, symmetric and antisymmetric boundary conditions together with the perfectly

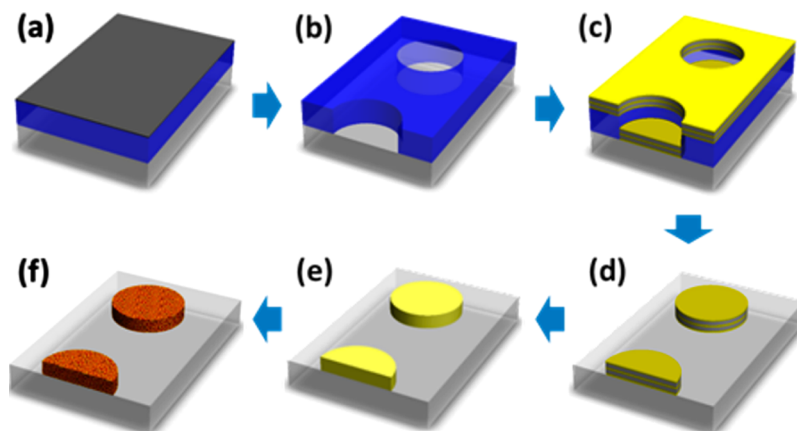
matched layer (PML) boundary can be applied. This reduces the calculation time and memory by a factor of 4 than that for the NP model. Besides, the 3D porous network for NP model requires longer meshing time and memory compared to that for the B-EMT model. For 500 nm disk model, the calculation time is ~ 1 and ~ 16 h, and the required memory is ~ 1 and ~ 25 GB for the B-EMT and NP models, respectively. Furthermore, the OST can be employed for the B-EMT model, which provides the extinction calculation almost instantaneously.

CONCLUSION

A fabrication method based on EBL technique is presented for NPG disks. This method is capable of providing orderly or randomly distributed NPG disks (also different arbitrary shapes and patterns) with required interparticle distance. Such fabrication flexibility enables us to obtain coupling free single NPG disk response using a common UV/vis/NIR spectrometer, which, otherwise, requires a specialized NIR spectroscopic microscope. Randomly distributed sparse NPG disk arrays (200–500 nm diameter and 50 nm thickness) with $\sim 6D$ interdisk distance are fabricated and characterized. Two different models, the B-EMT model and NP model, are developed for the NPG disk to calculate its plasmonic properties. The B-EMT model is very simple to build and does not require any information about the porous network. However, the NP model contains the 3D nanoporous architecture of the NPG. The performances of these models are evaluated by comparing the calculated plasmon resonance wavelength (λ_{LSPR})/energy (E_{LSPR}) and peak width (fwhm)/plasmon lifetime (T) with the experimental observations. Both the B-EMT and NP models provide almost the exact estimations for $\lambda_{\text{LSPR}}/E_{\text{LSPR}}$. However, the B-EMT model fails to provide the accurate information about the fwhm/ T and plasmonic hot-spots formation due to the absence of the porous network. The nanoporous architecture plays a significant role in plasmon damping and local e-field enhancement. The pore–ligament mesh increases the collision phenomenon for the oscillating electrons, thereby resulting in the enhanced plasmon damping, shorter plasmon lifetime, and wider plasmon peak. The 3D porous network provides the high density internal plasmonic hot-spots which is absent in the B-EMT model. The B-EMT model is simple, fast, requires less memory, and can even be used in analytical calculation method. However, to understand the plasmon peak width/lifetime, damping, and plasmonic hot-spots formation, the NP model is indispensable, which requires longer calculation time and larger memory.

METHODS

EBL Fabrication of NPG Disks. NPG disks of tightly controlled size and distribution were fabricated on glass substrates according to the schematic representation in Scheme 1a–f. At first, the glass substrate was spin coated with 200 nm poly methyl methacrylate (PMMA), followed by electron beam (e-beam) evaporation of 10 nm thick Cr overcoat to prevent the charging effect during EBL (Scheme 1a). Python software was used to generate a random array of circular shapes with average center to center distance of $6D$, where D denotes the disk diameter. The nanodisks were approximated by polygons, where the number of corners in the polygon was adjusted to the nanodisk size (ranging from dodecagons (200 and 300 nm) to hexadecagons (400 and 500 nm)). The samples were

Scheme 1. Schematic of NPG Disk Fabrication^a

^a(a) Cr-coated PMMA on glass substrate; (b) Developed PMMA after e-beam exposure and Cr removal; (c) Au–Ag multilayer depositions; (d) Au–Ag multilayer nanodisks; (e) Ag–Au alloy disk; and (f) NPG disk after de-alloying in nitric acid.

exposed in a JBX-5500 electron-beam lithography system at 50 kV accelerating voltage and 1 nA beam current. Square areas of roughly 3 mm² were patterned for each considered nanodisk size. After the e-beam exposure, the Cr layer was removed by dipping the samples in Cr etchant solution (Sigma-Aldrich) for 15 s, followed by extensive rinsing with ultrapure water and finally blow drying with nitrogen. Exposed samples were developed in mixture of water and isopropyl alcohol in a 1:3 ratio for 60 s (Scheme 1b). Next, 2 nm Ti was deposited by e-beam evaporation followed by multilayer depositions of alternating Au (4 nm) and Ag (13 nm) (Scheme 1c). The deposition thickness was measured by a crystal monitor in the e-beam tool. The multilayer deposition scheme, instead of the bilayer, was used to ensure uniform porous network across the disk thickness, which has been explained in detail in the Supporting Information. After the deposition, the PMMA resist and metal atop were removed via lift-off in acetone (24 h) to reveal Au–Ag multilayer nanodisks (Scheme 1d). The multilayer nanodisks were then annealed at 400 °C for 30 min to obtain the Ag–Au alloy disks (Scheme 1e). The thickness of the alloy disks was ~76 nm with ~30% Au gold volume fraction. Finally, randomly distributed NPG disks were obtained by dealloying the alloy disks in 70% nitric acid for 1 min followed by extensive rinsing and drying (Scheme 1f). The thickness of the NPG disks was ~50 nm (obtained by the SEM and AFM characterizations). The XPS surface compositional analysis reveals that the residual silver is ~8% (Supporting Information). Fabrication of NPG structures of “square”, “hollow-square”, and “triangular” shapes and “UH” pattern follow the similar methodology, except for the computer-generated design to be printed on the PMMA resist layer. Although the PMMA resist patterning technique is similar to that by Zoric et al.,¹⁴ this fabrication methodology provides a new approach to fabricate porous nanoparticles, with precise shape, size, and position control, utilizing the multilayer Au/Ag deposition, annealing, and subsequent dealloying techniques.

B-EMT Model. Although the NPG disk contains a very small amount (~8%) of residual silver, it is considered to be made of only the gold ligaments and air pores for simplicity of the modeling. Thus, the B-EMT model for NPG disk can be mathematically expressed as

$$(1 - \delta_{\text{air}}) \frac{\epsilon_{\text{Au}} - \epsilon_{\text{NPGD}}}{\epsilon_{\text{Au}} + 2\epsilon_{\text{NPGD}}} + \delta_{\text{air}} \frac{\epsilon_{\text{air}} - \epsilon_{\text{NPGD}}}{\epsilon_{\text{air}} + 2\epsilon_{\text{NPGD}}} = 0 \quad (5)$$

In eq 5, ϵ_{NPGD} is the effective permittivity of NPG disk, ϵ_{Au} and ϵ_{air} are the permittivity of gold and air, respectively, and δ_{air} is the porosity or air volume fraction. δ_{air} can be calculated using eq 6 under the assumption of complete removal and preservation of silver and gold, respectively, during the dealloying process.

$$\delta_{\text{air}} = \frac{1 - \delta_{\text{dealloy}} - \delta_{\text{Au}}}{1 - \delta_{\text{dealloy}}} \quad (6)$$

$$\delta_{\text{dealloy}} = \frac{V_{\text{alloy disk}} - V_{\text{NPGD}}}{V_{\text{alloy disk}}} \quad (7)$$

In eq 6, δ_{Au} is the Au volume fraction in Ag–Au alloy disk and δ_{dealloy} is the volume fraction reduction due to dealloying process. Due to the existence of the adhesion layer, there was no diameter shrinkage. However, the thickness was reduced from ~76 to ~50 nm. This gives $\delta_{\text{dealloy}} \approx 0.34$, which yields $\delta_{\text{air}} \approx 0.54$. The calculated δ_{air} is consistent with the previously reported air volume fraction which ranges from 0.3 to 0.65 for NPG films.^{31,32} Besides B-EMT, the Maxwell-Garnett effective medium theory (MG-EMT) can also be employed to model the NPG nanostructure. For example, Jiao et al. used the MG-EMT to estimate the porosity of patterned NPG substrate.³² However, the MG-EMT provides good approximation as long as the inclusion volume fraction is below 30%.^{33,34} When the volume fractions of the constituents are comparable in a composite material, the B-EMT is preferable.³⁴ The comparable volume fractions of air (0.54) and gold (0.46) in NPG disk thus justify the use of B-EMT over MG-EMT.

NP Model. The NP model is obtained by utilizing the 2D SEM images of NPG film of comparable dimensions. The modeling relies on the following assumptions: the 3D NPG structure can be roughly classified into ligament dominating layer (Au-rich layer) and pore dominating layer (air-rich layer) and these two types of layers alternate. Such assumptions are important for ensuring the bicontinuous nanostructures of NPG.³⁵ For the ligament dominating layer, the tube-like ligaments are extended horizontally to form 3D meshes with pores in-between the ligaments. As for the pore dominating

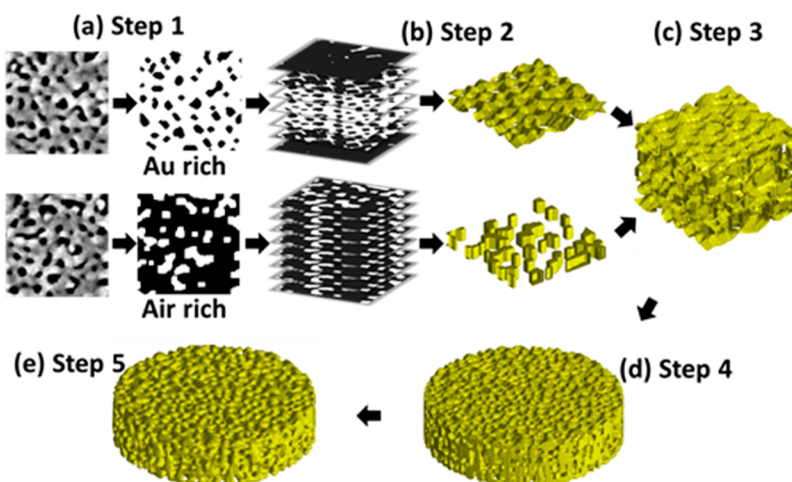


Figure 9. NP model of NPG disk: (a) step 1, binarization of 2D SEM images; (b) step 2, stacking of binarized images; (c) step 3, stacking of layers into NPG film; (d) step 4, disk cutting; (e) step 5, surface smoothing of as-generated NPG disk.

layer, the ligaments are extended vertically and appear to be suspended in air (porous region). Figure 9a–e show the stepwise schematic representations for generating the NP model of NPG disk. SEM images are binarized into Au-rich and air-rich images via different threshold values, as shown in Figure 9a. The binarized images are stacked into 3D ligaments, as shown in Figure 9b. For the ligament dominating layer, nearby images are generated by gradual increase in the pore area (black part), while for pore dominating layer, same images are stacked without modification. These layers are then alternated and stacked into a thicker NPG film as shown in Figure 9c. During stacking, the layers are intentionally overlapped (roughly 20%) to ensure the pore-ligament continuity. In our study, 75 nm thick NPG film is generated with five ligament dominating and four pore dominating layers. Then NPG disks with desired diameter and thickness are cut out from this film, as shown in Figure 9d. The generated NPG disk model has many sharp edges which are rounded by surface smoothing as shown in Figure 9e. The surface smoothing is done with “smooth3” command in MatLab, with a “box” convolution kernel of size 5 (i.e., $A = \text{smooth3}(A, \text{“box”}, 5)$, A being the NP model). The obtained NP model has random bicontinuous pore-ligament network as shown in the cross section movies provided in the Supporting Information (visualizations 1 and 2). The NP model of NPG disk has porosity (δ_{air}) in the range of 52–54%.

Optical Extinction Spectroscopy. Extinction measurements were performed on a Cary 5000 spectrophotometer. The full width at half-maximum (fwhm) of an extinction spectrum was determined by multiplying the peak half-width by a factor of 2. The peak half-width was measured from the resonance maximum toward the lower energy side due to the probable existence of multipolar resonance modes at the higher energy side.

Calculation Methods. Both numerical finite difference time domain (FDTD) method and analytical oblate spheroid theory (OST) were used in this study. Details of these methods and simulation setup can be found in the Supporting Information. All the calculations were done for single NPG disk. For OST calculations, the substrate effect was considered by assuming NPG disks embedded in a homogeneous medium whose refractive index is the average of air ($n = 1.00$) and the glass substrate ($n = 1.52$). The dielectric functions of Au were obtained from the literature.²⁶

■ ASSOCIATED CONTENT

§ Supporting Information

The Supporting Information is available free of charge on the ACS Publications website at DOI: 10.1021/acsp Photonics.7b00239.

(I) Multilayer Ag/Au deposition technique; (II) XPS analysis; (III) Random bi-continuous pore-ligament network of NP-model; (IV) Oblate spheroid theory (OST); (V) Finite difference time domain (FDTD) method; (VI) FDTD simulation setup; (VII) Derivation of MLWA polarizability for NPG disk (VIII) 3D E-field distribution (PDF).

Visualization 1: movie showing the random bi-continuous pore-ligament network of the NP model along the disk diameter (x – y cross-section) across the disk height at 1 nm step size (AVI).

Visualization 2: movie showing the random bi-continuous pore-ligament network of the NP model along the disk height (x – z cross-section) across the disk diameter at 1 nm step size (AVI).

Visualization 3: movie showing the e-field distributions for the NP model/ FDTD calculation along the disk diameter (x – y cross-section) across the disk height at 1 nm step size (AVI).

Visualization 4: movie showing the e-field distributions for the NP model/ FDTD calculation along the disk height (x – z cross-section) across the disk diameter at 5 nm step size (AVI).

■ AUTHOR INFORMATION

Corresponding Author

*E-mail: wshih@uh.edu.

ORCID

Wei-Chuan Shih: 0000-0002-7530-7352

Author Contributions

[†]M.M.P.A. and F. Z. contributed equally to this work.

Notes

The authors declare no competing financial interest.

ACKNOWLEDGMENTS

This work was partially funded by the following grant and contracts: National Science Foundation (NSF) CAREER Award 1151154, NSF 1605683, and Department of Interior, Bureau of Safety and Environmental Enforcement (BSEE-1040).

REFERENCES

- (1) Rosi, N. L.; Mirkin, C. A. Nanostructures in Biodiagnostics. *Chem. Rev.* **2005**, *105*, 1547–1562.
- (2) McConnell, W. P.; Novak, J. P.; Brousseau, L. C.; Fuierer, R. R.; Tenent, R. C.; Feldheim, D. L. Electronic and Optical Properties of Chemically Modified Metal Nanoparticles and Molecularly Bridged Nanoparticle Arrays. *J. Phys. Chem. B* **2000**, *104*, 8925–8930.
- (3) Zhao, F.; Zeng, J.; Parvez Arnob, M. M.; Sun, P.; Qi, J.; Motwani, P.; Gheewala, M.; Li, C.-H.; Paterson, A.; Strych, U.; Raja, B.; Willson, R. C.; Wolfe, J. C.; Lee, T. R.; Shih, W.-C. Monolithic NPG nanoparticles with large surface area, tunable plasmonics, and high-density internal hot-spots. *Nanoscale* **2014**, *6*, 8199–8207.
- (4) Arnob, M. M. P.; Zhao, F.; Zeng, J.; Santos, G. M.; Li, M.; Shih, W.-C. Laser rapid thermal annealing enables tunable plasmonics in nanoporous gold nanoparticles. *Nanoscale* **2014**, *6*, 12470–12475.
- (5) Shih, W.-C.; Santos, G. M.; Zhao, F.; Zenasni, O.; Arnob, M. M. P. Simultaneous Chemical and Refractive Index Sensing in the 1–2.5 μm Near-Infrared Wavelength Range on Nanoporous Gold Disks. *Nano Lett.* **2016**, *16*, 4641–4647.
- (6) Li, M.; Du, Y.; Zhao, F.; Zeng, J.; Mohan, C.; Shih, W.-C. Reagent- and separation-free measurements of urine creatinine concentration using stamping surface enhanced Raman scattering (S-SERS). *Biomed. Opt. Express* **2015**, *6*, 849–858.
- (7) Santos, G. M.; Zhao, F.; Zeng, J.; Li, M.; Shih, W.-C. Label-free, zeptomole cancer biomarker detection by surface-enhanced fluorescence on nanoporous gold disk plasmonic nanoparticles. *J. Biophotonics* **2015**, *8*, 855–863.
- (8) Santos, G. M.; Ferrara, F. I. d. S.; Zhao, F.; Rodrigues, D. F.; Shih, W.-C. Photothermal inactivation of heat-resistant bacteria on nanoporous gold disk arrays. *Opt. Mater. Express* **2016**, *6*, 1217–1229.
- (9) Qi, J.; Motwani, P.; Gheewala, M.; Brennan, C.; Wolfe, J. C.; Shih, W.-C. Surface-enhanced Raman spectroscopy with monolithic nanoporous gold disk substrates. *Nanoscale* **2013**, *5*, 4105–4109.
- (10) Liu, K.; Bai, Y.; Zhang, L.; Yang, Z.; Fan, Q.; Zheng, H.; Yin, Y.; Gao, C. Porous Au–Ag Nanospheres with High-Density and Highly Accessible Hotspots for SERS Analysis. *Nano Lett.* **2016**, *16*, 3675–3681.
- (11) Rao, W.; Wang, D.; Kups, T.; Baradács, E.; Parditka, B.; Erdélyi, Z.; Schaaf, P. Nanoporous Gold Nanoparticles and Au/Al₂O₃ Hybrid Nanoparticles with Large Tunability of Plasmonic Properties. *ACS Appl. Mater. Interfaces* **2017**, *9* (7), 6273–6281.
- (12) Vidal, C.; Wang, D.; Schaaf, P.; Hrelescu, C.; Klar, T. A. Optical Plasmons of Individual Gold Nanosponges. *ACS Photonics* **2015**, *2*, 1436–1442.
- (13) Olson, J.; Dominguez-Medina, S.; Hoggard, A.; Wang, L.-Y.; Chang, W.-S.; Link, S. Optical characterization of single plasmonic nanoparticles. *Chem. Soc. Rev.* **2015**, *44*, 40–57.
- (14) Zorić, I.; Zäch, M.; Kasemo, B.; Langhammer, C. Gold, Platinum, and Aluminum Nanodisk Plasmons: Material Independence, Subradiance, and Damping Mechanisms. *ACS Nano* **2011**, *5*, 2535–2546.
- (15) Hanarp, P.; Käll, M.; Sutherland, D. S. Optical Properties of Short Range Ordered Arrays of Nanometer Gold Disks Prepared by Colloidal Lithography. *J. Phys. Chem. B* **2003**, *107*, 5768–5772.
- (16) Wang, D.; Schaaf, P. Nanoporous gold nanoparticles. *J. Mater. Chem.* **2012**, *22*, 5344–5348.
- (17) Wi, J.-S.; Tominaka, S.; Uosaki, K.; Nagao, T. Porous gold nanodisks with multiple internal hot spots. *Phys. Chem. Chem. Phys.* **2012**, *14*, 9131–9136.
- (18) Sardana, N.; Heyroth, F.; Schilling, J. Propagating surface plasmons on nanoporous gold. *J. Opt. Soc. Am. B* **2012**, *29*, 1778–1783.
- (19) Dixon, M. C.; Daniel, T. A.; Hieda, M.; Smilgies, D. M.; Chan, M. H.; Allara, D. L. Preparation, structure, and optical properties of nanoporous gold thin films. *Langmuir* **2007**, *23*, 2414–2422.
- (20) Ngô, B.-N. D.; Stukowski, A.; Mameka, N.; Markmann, J.; Albe, K.; Weissmüller, J. Anomalous compliance and early yielding of nanoporous gold. *Acta Mater.* **2015**, *93*, 144–155.
- (21) Erlebacher, J.; Aziz, M. J.; Karma, A.; Dimitrov, N.; Sieradzki, K. Evolution of nanoporosity in dealloying. *Nature* **2001**, *410*, 450–453.
- (22) Xia, R.; Wu, R. N.; Liu, Y. L.; Sun, X. Y. The Role of Computer Simulation in Nanoporous Metals—A Review. *Materials* **2015**, *8*, 5060–5083.
- (23) Lang, X.; Guan, P.; Zhang, L.; Fujita, T.; Chen, M. Characteristic length and temperature dependence of surface enhanced Raman scattering of nanoporous gold. *J. Phys. Chem. C* **2009**, *113*, 10956–10961.
- (24) Arnob, M. M. P.; Zhao, F.; Shih, W. C. In Modeling nanoporous gold plasmonic nanoparticles: Calculation of optical properties. *IEEE-NANO* **2015**, *15*, 29–32.
- (25) Zhang, Q.; Large, N.; Nordlander, P.; Wang, H. Porous Au Nanoparticles with Tunable Plasmon Resonances and Intense Field Enhancements for Single-Particle SERS. *J. Phys. Chem. Lett.* **2014**, *5*, 370–374.
- (26) Johnson, P. B.; Christy, R.-W. Optical constants of the noble metals. *Phys. Rev. B* **1972**, *6*, 4370.
- (27) Sönnichsen, C.; Franzl, T.; Wilk, T.; von Plessen, G.; Feldmann, J.; Wilson, O.; Mulvaney, P. Drastic Reduction of Plasmon Damping in Gold Nanorods. *Phys. Rev. Lett.* **2002**, *88*, 077402.
- (28) Sönnichsen, C. Plasmons in metal nanostructures. *Ph.D. dissertation*, Ludwig-Maximilians-University of Munich, Munich, Germany, 2001.
- (29) Sonnefraud, Y.; Verellen, N.; Sobhani, H.; Vandenbosch, G. A. E.; Moshchalkov, V. V.; Van Dorpe, P.; Nordlander, P.; Maier, S. A. Experimental Realization of Subradiant, Superradiant, and Fano Resonances in Ring/Disk Plasmonic Nanocavities. *ACS Nano* **2010**, *4*, 1664–1670.
- (30) Hägglund, C.; Zäch, M.; Petersson, G.; Kasemo, B. Electromagnetic coupling of light into a silicon solar cell by nanodisk plasmons. *Appl. Phys. Lett.* **2008**, *92*, 053110.
- (31) Seker, E.; Gaskins, J. T.; Bart-Smith, H.; Zhu, J.; Reed, M. L.; Zangari, G.; Kelly, R.; Begley, M. R. The effects of post-fabrication annealing on the mechanical properties of freestanding nanoporous gold structures. *Acta Mater.* **2007**, *55*, 4593–4602.
- (32) Jiao, Y.; Ryckman, J. D.; Koktysh, D. S.; Weiss, S. M. Controlling surface enhanced Raman scattering using grating-type patterned nanoporous gold substrates. *Opt. Mater. Express* **2013**, *3*, 1137–1148.
- (33) Spanoudaki, A.; Pelster, R. Effective dielectric properties of composite materials: The dependence on the particle size distribution. *Phys. Rev. B: Condens. Matter Mater. Phys.* **2001**, *64*, 064205.
- (34) Wenshan Cai, V. S. *Optical Metamaterials Fundamentals and Applications*; Springer: New York, 2010.
- (35) Ding, Y.; Kim, Y. J.; Erlebacher, J. Nanoporous gold leaf: “Ancient technology”/advanced material. *Adv. Mater.* **2004**, *16*, 1897–1900.